Journal of Materials Chemistry A

ROYAL SOCIETY OF CHEMISTRY

COMMUNICATION

View Article Online
View Journal | View Issue

Cite this: J. Mater. Chem. A, 2025, 13, 36953

Received 9th August 2025
Accepted 13th October 2025

DOI: 10.1039/d5ta06459g

rsc.li/materials-a

Hydrazine-free precursor for solution-processed all-inorganic Se and $Se_{1-x}Te_x$ photovoltaics

Adam D. Alfieri, [a] Swarnendu Das, [b] Kim Kisslinger, [c] Brian M. Everhart,[d] Chloe Leblanc, [a] Jamie Ford,[e] Cherie R. Kagan, [abf] Nicholas R. Glavin, [d] Eric A. Stach [b] and Deep Jariwala *[a]

Selenium (Se) has reemerged as a promising absorber material for indoor and tandem photovoltaics (PVs), and its alloys with Te ($Se_{1-x}Te_x$) offer a widely tunable bandgap. Solution processing of this materials system offers a route to low-cost fabrication. However, solution processing of Se has, thus far, only used hydrazine, which is an extremely hazardous solvent. In this work, we prepare and isolate propylammonium poly-Se and poly-Se–Te precursors from a safer thiol-amine solvent system. We formulate molecular inks by dissolving the precursor in dimethylformamide (DMF) with a monoethanolamine (EA) additive and process high-quality Se and $Se_{1-x}Te_x$ films with bandgaps ranging from 1.20 eV to 1.86 eV. We fabricate PVs from these films using TiO_2 and MoO_3 charge transport layers (CTLs) to achieve power conversion efficiencies as high as 2.73% for Se and 2.33% for $Se_{0.7}Te_{0.3}$ under solar simulation. Se devices show excellent stability with no degradation after 1 month in air, enabled by the excellent stability of Se and the use of inorganic CTLs. This work represents an important step towards low-cost solution-phase processing of Se and $Se_{1-x}Te_x$ alloys for PVs and photodetectors with low toxicity and high bandgap tunability.

Introduction

The world's first PV material, trigonal Se,[1] has experienced a renaissance as a promising absorber material for both tandem and indoor PVs,[2–5] with PCEs of 8.1% achieved under AM1.5G illumination[6] and over 26% PCE under indoor lighting,[7] surpassing commercial amorphous-Si:H for this application. Se exhibits strong absorption, good carrier mobility, low toxicity, and a unique combination of low processing temperatures and stability. An added benefit of Se is its broad tunability through isomorphic alloying with Te, enabling the alloy bandgap to be tuned from 0.3 eV to 1.9 eV with just 2 elements and attracting some attention for optoelectronics.[8–11] Typically, Se is processed by thermal evaporation, limiting throughput and increasing costs. Given the low melting point of Se (217 °C), melt processing has been successfully pursued,[7,12] but this is difficult to control and results in excessively thick (>2 μm) films that lead to material waste. Solution processing is an alternative approach that offers significantly higher throughput and lower capital costs than vacuum processing with less material consumption than melt processing, driving down manufacturing costs.

Solution processing of Se PVs has been shown using hydrazine,[13,14] which is an effective but extremely hazardous solvent, limiting both widespread research and eventual commercialization using this method. Instead, elemental Se and Te can be dissolved in the thiol-amine solvent system,[15] which is far safer than hydrazine. $Se_{0.7}Te_{0.3}$ films for solar cells were prepared from an ethylenediamine:ethanethiol (EDA:ET) solvent at temperatures ≤200 °C, with a device efficiency of 1.1%.[10] Thiol-amine processed Se and $Se_{1-x}Te_x$ PVs are therefore worth pursuing for scalable production of stable PVs for indoor and solar applications. However, thiol-amine processing has yet to be applied to pure Se cells, and further development of thiol-amine-based precursors is needed.

Thiol-amine processing of Se and Te has primarily focused on metal selenides and metal tellurides.[16] It was found that dissolving Se in alkylamine:ET (AA:ET) creates an alkylammonium poly-selenide (AAPSe) species that acts as an "alkahest"[17] capable of dissolving a variety of metals. The AAPSe alkahest was shown to be able to dissolve Te, which is insoluble in AA:ET solutions in the absence of Se.[18] Changing the amine (AA *vs.* EDA) impacts the precursor. Given the importance of precursor selection to the morphology and performance of solution processed thin film PVs, identifying a precursor most suitable for

[a]*Electrical and Systems Engineering, University of Pennsylvania, Philadelphia, PA, 19104, USA. E-mail: dmj@seas.upenn.edu*

[b]*Materials Science and Engineering, University of Pennsylvania, Philadelphia, PA, 19104, USA*

[c]*Center for Functional Nanomaterials, Brookhaven National Laboratory, Upton, NY, 11973, USA*

[d]*Air Force Research Laboratory, Materials and Manufacturing Directorate, Wright-Patterson Air Force Base, Fairborn, OH, 45433, USA*

[e]*Singh Center for Nanotechnology, University of Pennsylvania, Philadelphia, PA, 19104, USA*

[f]*Chemistry, University of Pennsylvania, Philadelphia, PA, 19104, USA*

producing films and then developing a process based on that precursor is a crucial first step towards solution processed Se and $Se_{1-x}Te_x$ PVs.

In this work, we use precursor and process engineering to control the morphology of Se and $Se_{1-x}Te_x$ films produced by thiol-amine processing. We demonstrate that propylammonium poly-selenide (PAPSe) and poly-$Se_{1-x}Te_x$ (PAPST) salts prepared from propylamine (PA) and ET can be redissolved in benign solvents and spin-coated on preheated substrates to achieve uniform, high-quality films of Se and $Se_{1-x}Te_x$ alloys with widely tunable bandgaps. We fabricate and characterize photovoltaics from the films and achieve a respectable PCE of 2.73% and open circuit voltage (V_{oc}) as high as 854 mV for Se, comparable to that of evaporated films. Similarly, we achieve 2.33% PCE for ~1.20 eV bandgap $Se_{0.7}Te_{0.3}$ films, which is more than double the previous report on solution processed $Se_{1-x}Te_x$ PVs.

Results

Precursor

We prepare two different precursors for pure Se, shown in Fig. 1, through the dissolution of elemental Se in two thiol-amine solvent systems. First, we consider dissolving Se in a PA/ET solvent system. This results in "dimensional reduction" of the Se chain to form short poly-selenide chains coordinated by propylammonium ions, similar to the Se species present when dissolved in hydrazine.[17,19] Deprotonated thiols react with each other to form diethyl disulfide (DEDS). Toluene is added to precipitate the propylammonium poly-selenide (PAPSe) salt. Toluene, DEDS, and excess unreacted amine/thiol are extracted by decanting the supernatant and vacuum drying. The solid PAPSe salt can then be dissolved in polar aprotic solvents. Alternatively, elemental Se is dissolved in EDA:ET, producing an ethanethio-poly-selenide (ETPSe) anion coordinated by the $H_2NC_2H_4NH_3^+$ cation in which the ethanethio-ligand is bonded to the poly-selenide chain. Here, excess EDA and ET are similarly extracted using toluene and vacuum, but the resulting compound is a viscous liquid that can be diluted with EDA or polar solvents. Both PAPSe and ETPSe can be converted to trigonal Se upon annealing (Fig. S1). Differences between diamine-thiol and monoamine-thiol precursors are discussed in more detail in another previous work.[18]

We make films by dissolving the PAPSe salt in DMF with a small (2% by volume) EA additive. The EA additive was found to increase grain size and improve device performance (Fig. S2), presumably due to the high boiling point and interaction with Se. Similarly, we dilute ETPSe precursor to approximately 4 M with DMF. The films are deposited by dynamic spin-coating of the solution on mesoporous- (mp-)TiO_2/compact- (c-)TiO_2/FTO/glass substrates preheated to 110 °C, converting to Se by annealing at 110 °C, and then crystallizing the films at 200 °C (see SI for Methods). We found that preheating the substrate to 110 °C resulted in greater reproducibility and film adhesion/uniformity compared to an unheated substrate and/or using an antisolvent, though antisolvent engineering could be a future path to control film nucleation and growth. Fig. 2a shows the camera image (top row) and corresponding SEM image (bottom row) of a representative Se film from ETPSe, and Fig. 2b shows the same for the Se film from PAPSe. We were

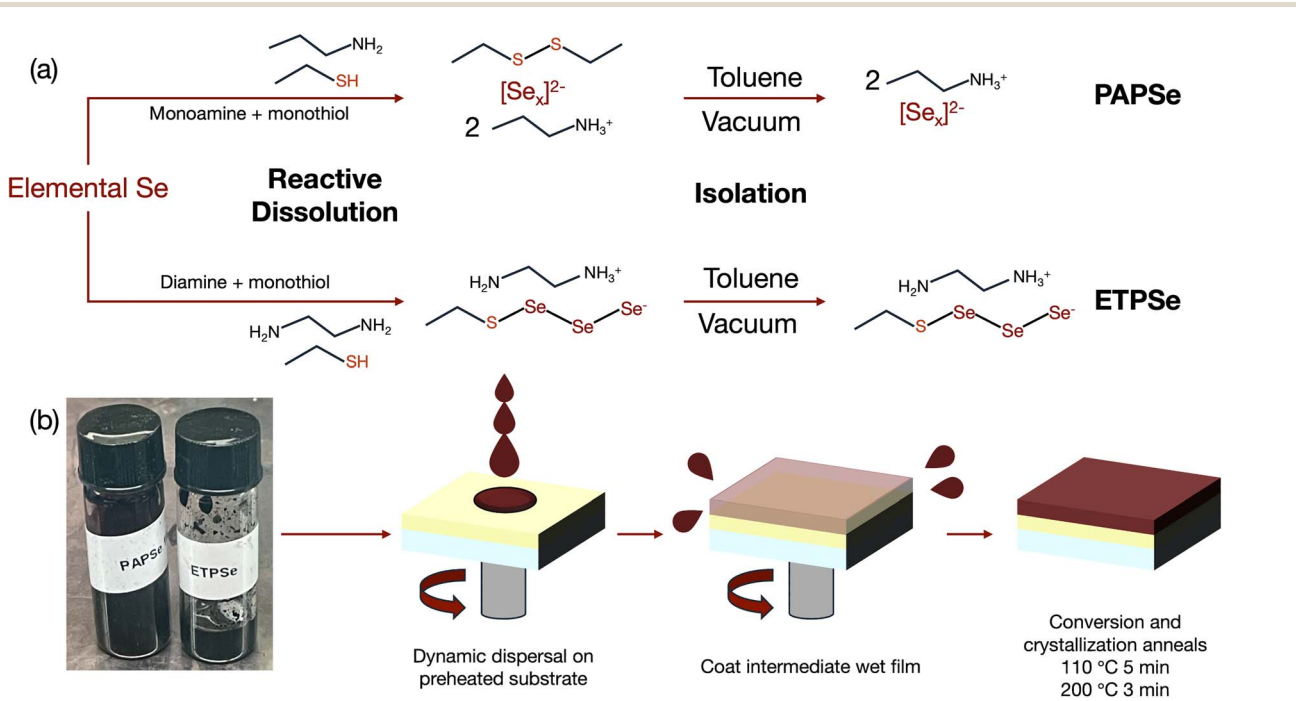

Fig. 1 Precursor chemistry and deposition process. (a) Dissolution of elemental Se in propylamine and ethanethiol results in a different precursor than dissolution in ethylenediamine and ethanethiol. Preparation of $Se_{1-x}Te_x$ alloys follows the same precursor form. (b) Images of PAPSe and ETPSe precursor inks and schematic of deposition process.

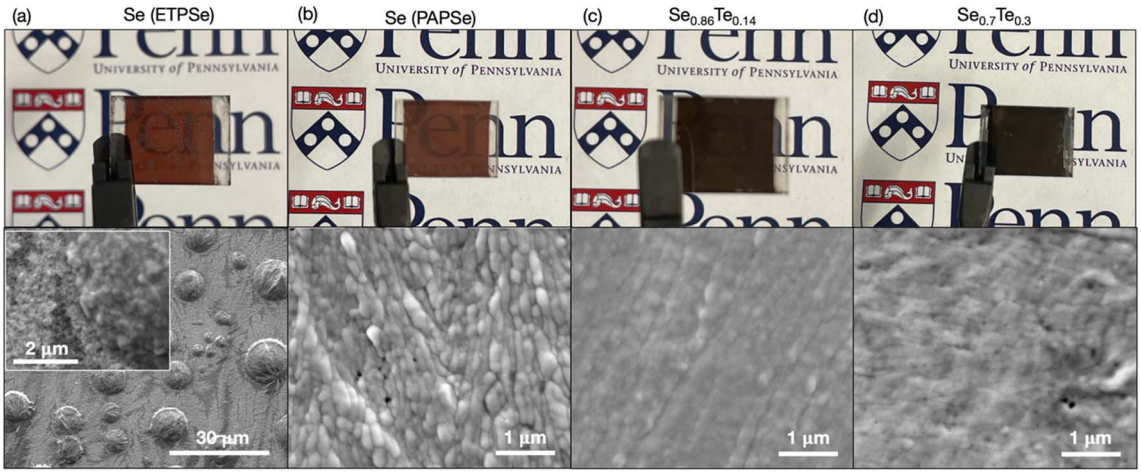

Fig. 2 Optical and Electron Microscope Images of Films. Camera (top row) and SEM (bottom row) images of (a) Se processed from ETPSe, (b) Se processed from PAPSe, (c) 14% Te, and (d) 30% Te films. The camera images are taken from the bottom side of the 20 mm × 15 mm TiO_2/FTO/glass substrate.

unable to achieve uniform films from ETPSe, as the precursor tends to form large discontinuous clusters on top of an infiltrated mp-TiO_2 layer instead of films. In contrast, PAPSe films are continuous, uniform, and have well defined grains with sizes on the order of several hundreds of nanometers, comparable to evaporated Se films with similar thicknesses.[3] The morphology is dense, except for small pinholes to the mp-TiO_2 that will need to be eliminated with process optimization. Overall, Se films from the PAPSe precursor clearly have a wider processing window than Se films from ETPSe, and we focus on PAPSe-processed films for the remainder of this work.

Alloying with Te

We also use the PA-based precursor to make $Se_{1-x}Te_x$ alloys using the same precursor chemistry by adding stoichiometric amounts of Se and Te powder during the precursor preparation, producing propylammonium poly-seleno-telluride (PAPST) salts. Precursors with Te concentrations of 10% and 20% Te were used, resulting in films with compositions of approximately 14% Te ($Se_{0.86}Te_{0.14}$) and 30% Te ($Se_{0.7}Te_{0.3}$), estimated by energy dispersive X-ray spectroscopy (EDX, Methods). Se loss is likely due to a combination of higher solubility of Se-rich precursor in the precursor ink and the higher vapor pressure of Se resulting in Se loss during annealing.[10] Camera and SEM images of the 14% and 30% Te films are shown in Fig. 2c and d. Adding Te results in strongly absorbing, smooth films (RMS roughness of 10.0 nm for 14% Te, 5.7 nm RMS roughness for 30% Te, Fig. S6) with significantly smaller grains (tens of nm) that are difficult to resolve. The decrease in grain size is consistent with previous observations[9] and the hypothesis that adding Te requires short chains.[20] The films produced from PAPST nonetheless highlight the potential and flexibility of this precursor system.

Fig. 3 shows cross-sectional scanning transmission electron microscopy (X-STEM) analysis of the $Se_{1-x}Te_x$ alloy films. Fig. 3a and b are high-angle annular dark field STEM (HAADF-STEM) images of the 14% and 30% devices completed with MoO_x and an Au electrode (the device structure is discussed later in the manuscript). The films are smooth and approximately 200 nm in thickness. It is additionally important to consider the homogeneity of the alloying. While evaporation from a single source precursor yields a compositional gradient due to the difference in vapor pressure of Se and Te,[9] EDX analysis of the 30% Te film confirms that the alloying in PAPST-processed films is homogenous (Fig. 3c). This is a clear advantage in solution processing $Se_{1-x}Te_x$ alloys from PAPST. Further, it is clear from the HAADF-STEM images and the EDX analysis that the $Se_{1-x}Te_x$ absorber completely infiltrates the mp-TiO_2 layer (Fig. 3c).

The bandgap as a function of Te concentration can be estimated using UV-Vis absorption spectroscopy. The absorbance for the various concentrations is plotted in Fig. 4a. The estimated bandgaps from fitting the absorbance are 1.83 eV for pure Se, 1.54 eV for 14% Te, and 1.25 eV for 30% Te, which are consistent with the bandgap determined from device external quantum efficiency (EQE) measurements: 1.86 eV, 1.48 eV, and 1.20 eV (Fig. 5e). This wide range of bandgap tunability using solution processing with just 2 elements and the same precursor chemistry makes this system attractive for indoor PVs, tandem top cells, single junction PVs, and near IR photodiodes.

Raman spectra for the 3 samples is shown in Fig. 4b. The sharp peak at 234 cm^{-1} is consistent with the trigonal phase, and the absence of a peak at 251 cm^{-1} for Se indicates the lack of an amorphous phase. The peak at 234 cm^{-1} can be deconvoluted into nearly degenerate E and A_1 modes, hence the shoulder on the peak. As Te is added, this peak gets weaker and broader, and it redshifts to 221 cm^{-1} for 30% Te. The 14% Te spectrum shows an emergence of a new mode at 197 cm^{-1} that redshifts to 186 cm^{-1} for 30% Te. A smaller Te lattice mode also emerges at 162 cm^{-1} in the 30% Te spectrum. These modes can be understood as multimode behavior of E and A_1 modes

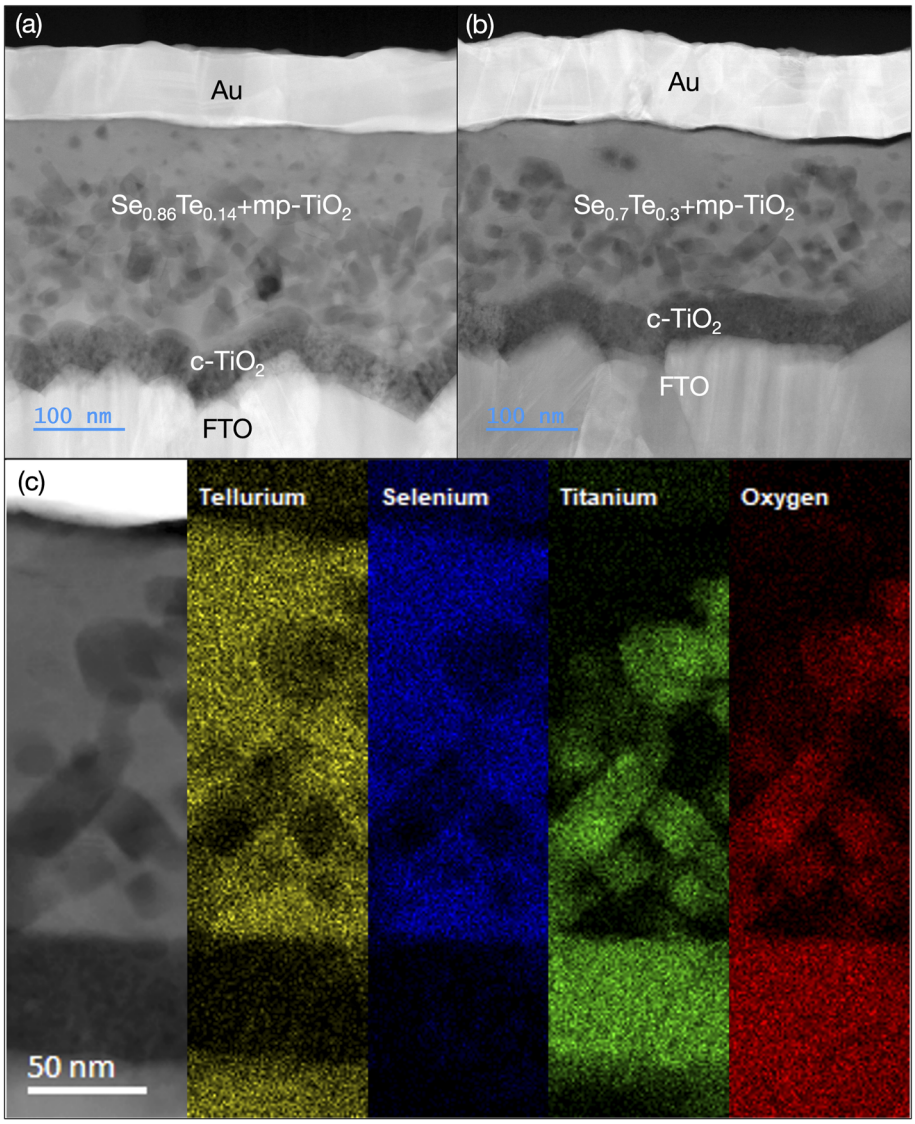

Fig. 3 Cross sectional scanning TEM (STEM) analysis. (a) High-Angle Annular Dark Field STEM (HAADF-STEM) images of (a) 14% Te and (b) 30% Te films, indicating absorber layer thicknesses of approximately 200 nm. The ultrathin MoO_x layer is present in all images but is not labeled in the images for readability. (c) X-STEM image and EDS maps of Te, Se, Ti, and O for the 30% Te film confirming uniform alloying and full infiltration of the mesoporous (mp)-TiO_2 layer.

emerging due to the large energy difference between the 2nd optical phonon bands for Se and Te.[21] The smaller peak that shifts from ~137 cm^{-1} for pure Se to 130 cm^{-1} for 30% Te is an *E* mode in the first optical phonon band. The composition-dependent positions of the peaks the alloy films are consistent with previous reports,[21] indicating that the compositions extracted from EDX are reasonable estimates despite the inherent uncertainty associated with EDX.

The XRD data (Fig. 4c) shows (100) and (101) diffraction peaks for Se, consistent with the desired trigonal phase. Because trigonal $Se_{1-x}Te_x$ films are composed of aligned 1D chains, the orientation of these chains in the film is important for charge transport and ultimately device performance.[6,22] It is desirable to have these 1D chains oriented out of plane, *i.e.*, maximize the ratio of the (101) peak to the (001) peak. The ratio of the desired (101) peak at ~29.7° to the (100) peak at ~23.6° for the Se film is comparable or superior to films produced by evaporation of Se with a Te interlayer on an unheated substrate. Further optimization of deposition conditions to achieve a fully (101) textured film will be beneficial for charge transport and device performance, and this should be a focus of future studies. The 14% Te film shows significantly smaller peaks, indicative of poor crystallinity. Interestingly, as the Te concentration increases to 30%, the crystallinity improves, but with an undesired (100) texture. The shifting of the peaks to lower angles with Te addition is consistent with previous results.[10] The large differences in the XRD spectra with varying Te content show that Te has a large effect on the nucleation and growth kinetics.

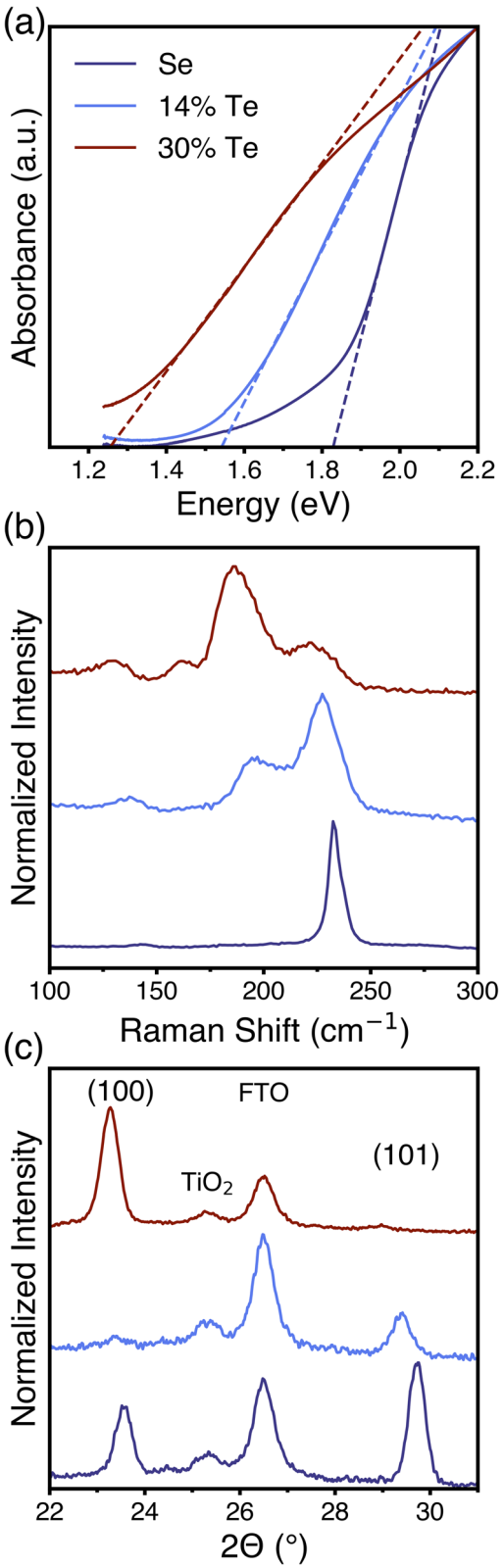

Fig. 4 Film characterization. (a) UV-Vis absorbance (b) Raman and (c) XRD for varying Te concentration. For this figure and those that follow, the dark blue curve corresponds to pure Se, the light blue corresponds to 14% Te, and the red curve corresponds to 30% Te.

Device performance

Devices are fabricated from the PAPST $Se_{1-x}Te_x$ films using the device structure in Fig. 5a: FTO/c-TiO_2/mp-TiO_2/$Se_{1-x}Te_x$/MoO_x/Au, where the TiO_2 is the electron transport layer (ETL) and the MoO_x layer is the hole transport layer (HTL). We note that the ability to use the inorganic, evaporated 15 nm MoO_x HTL is enabled by the uniformity of our films. Using MoO_x instead of doped PTAA or spiro-OMeTAD (as in other prior works[10,13]) will enable significantly greater long-term stability and lower costs. Fig. 5b shows a cross-sectional SEM image indicating that the film thickness is approximately 285 nm for Se. The $Se_{1-x}Te_x$ films are approximately 200 nm thick (Fig. 3a and b).

Fig. 5c shows the *J–V* curves under simulated AM1.5G light (intensity of 93.4 mW cm^{-2}) with an LED based solar simulator (Methods). Fig. 4f shows the statistics for the device efficiency of Se and alloy cells; full device statistics (including J_{sc}, V_{oc}, and FF) are provided in Fig. S3, and the maximum and mean values of J_{sc}, V_{oc}, FF, and PCE are listed in Table 1. Pure Se cells initially showed a PCE as high as 2.48%. After aging the devices in air (in the dark) and re-measuring, the PCE improves to 2.73%. The improvement after aging has been previously observed for Se devices with a MoO_x HTL.[23] While the overall efficiency is lower than evaporated Se PVs and one report of hydrazine-processed Se PVs, our Se cells exhibit an open circuit voltage (V_{oc}) as high as 854 mV, ~200 mV better than cells processed with hydrazine and only ~100 mV less than the best evaporated Se PVs. However, our devices exhibit significantly lower short circuit current density (J_{sc}), ultimately resulting in worse efficiencies. The short circuit current density is comparable to Te-free interfaces in evaporated cells,[4] suggesting that the interface could be a limiting factor. C–V analysis (Fig. S4) indicates that the defect density is in the range of 10^{18} cm^{-3}. However, this is almost entirely due to interface states, as drive-level capacitance measurements – which minimize interfacial contributions[24] – give bulk defect densities as low as 5.9×10^{16} cm^{-3} (Fig. S4), which is only one order of magnitude higher than state-of-the-art evaporated cells.[25] Despite the efficiency deficit, the comparable V_{oc} of PAPSe-processed Se photovoltaics to evaporated films suggests that PAPSe-processed Se devices have the potential to reach similar or even improved efficiencies with greater understanding and optimization of the film processing and the buried interface, which should be a strong focus for future research and development in the community.

The devices from alloyed films show a drastic decrease in V_{oc} and FF, but the J_{sc} is enhanced, particularly for 30% Te, which approaches a J_{sc} of 20 mA cm^{-2} in a 200 nm thick film. This trend has been previously seen in evaporated $Se_{1-x}Te_x$ PVs.[9] The best 30% and 14% devices have PCEs of 2.33% and 1.70%, respectively. There is significant difference in the performance between 14% and 30% Te despite the bandgaps, 1.5 eV and 1.2 eV, both being in the approximately optimal range for single junction PVs, which we assume to be related to the improved crystallinity of the 30% Te film. This suggests that there is significant room for optimization of single junction $Se_{1-x}Te_x$ PVs by composition within the ideal bandgap window. The champion alloy PCE 2.33% doubles the efficiency of the

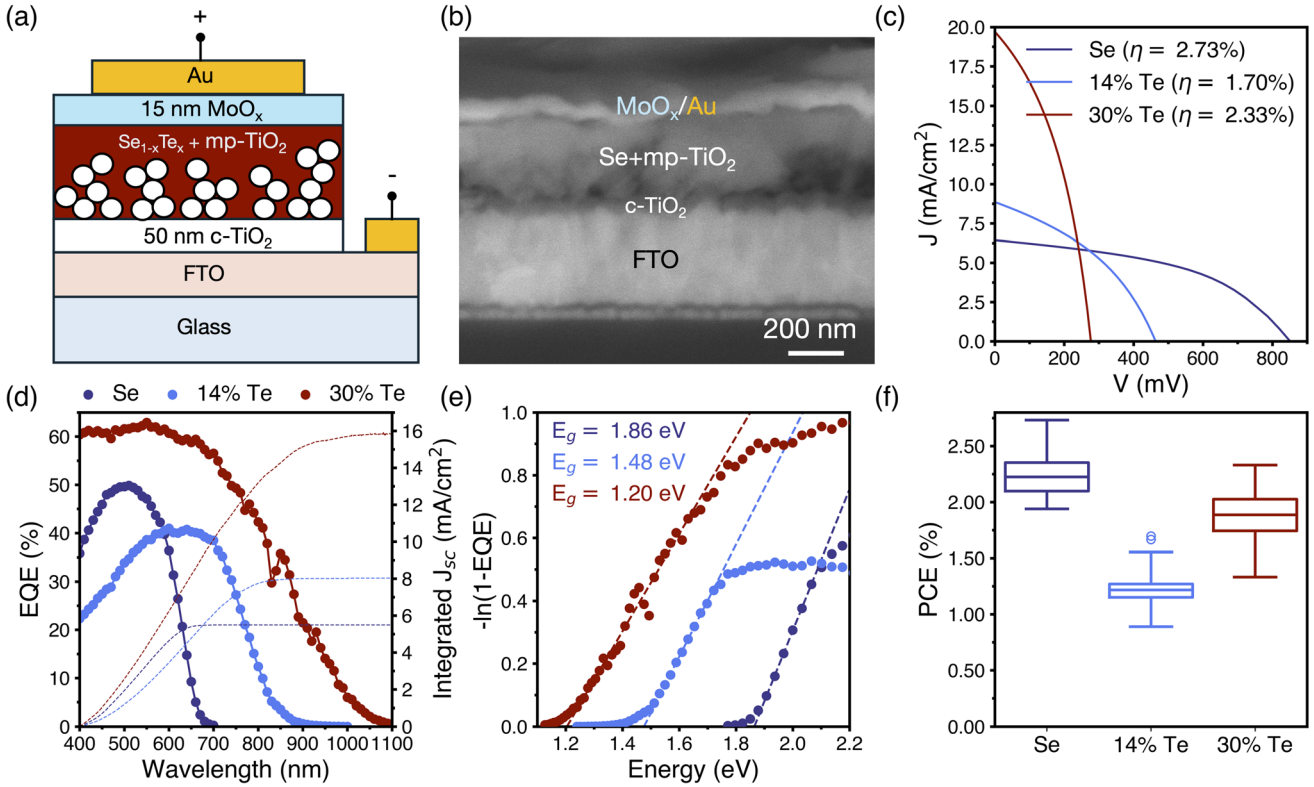

Fig. 5 Photovoltaic device performance. (a) Device structure schematic and (b) cross sectional SEM image of a Se device. Devices have a mesoscopic superstrate configuration with a TiO_2 electron transport layer and a MoO_x hole transport layer. (c) *J*–*V* curves of devices from different Te concentrations. (d) EQE spectra (scatter plots) with integrated short circuit current density (dashed lines) for different Te concentrations. The measurement is only conducted from 400–1100 nm. (e) −ln(1-EQE) spectra for different Te concentrations with bandgaps extracted and listed. (f) Boxplot of the PCE as a function of Te concentration. To account for device aging, the *J*–*V* scan with the highest PCE from each device over time is included in the boxplot.

Table 1 Champion (mean) device characteristics for PVs from Se and various Te concentrations

Material	J_{sc} (mA cm^{-2})	V_{oc} (mV)	FF (%)	PCE (%)
Se	6.6 (5.7)	854 (824)	50.1 (47.3)	2.73 (2.24)
14% Te	8.8 (6.8)	502 (445)	42.7 (40.4)	1.70 (1.24)
30% Te	19.8 (16.4)	304 (269)	44.1 (42.2)	2.33 (1.87)

previous report on solution processed $Se_{1-x}Te_x$ cells,[10] and is approaching the efficiency of the best evaporated $Se_{1-x}Te_x$ cells.[9] This value is comparable to other novel lead-free technologies and not especially impressive, but the bandgap tunability, low toxicity, and facile low-temperature processing makes the $Se_{1-x}Te_x$ system worth further exploration. It is also worth mentioning that while Te is a scarce element, a ~200 nm thick absorber layer (including the TiO_2 scaffold), 30% Te absorber could still be more sustainably scalable than other established thin film PV technologies with scarce elements and thicknesses of several microns, *e.g.* Cu(In,Ga)S_2 and CdTe.

Fig. 5d shows the EQE spectra of representative devices with varying Te concentration. EQE values reach a maximum of approximately 50% for pure Se. The drop in EQE at shorter wavelengths may be the result of interfacial recombination. The addition of Te extends the spectral response, as can be expected from the UV-Vis data. The 30% Te spectrum achieves maximum EQE values approaching 60% in the visible regime and exhibits a spectral response extending beyond 900 nm. The EQE begins to drop at wavelengths of 700 nm and longer, which is possibly the result of either incomplete absorption in this range or poor long wavelength photon collection due to recombination in the space-charge region. Integrating the J_{sc} values using a standard AM1.5G spectrum gives values of 5.5, 8.0, and 15.9 mA cm^{-2}, comparable to J_{sc} values of 6.2, 7.0, and 16.0 mA cm^{-2} for these specific devices measured under solar simulation. Discrepancies can be attributed to a combination of the wavelength regime below 400 nm being excluded (see Methods), spectral mismatch between the solar simulator and the AM1.5G spectrum, misalignment within the homebuilt system, effects of low light intensity, *etc.* The bandgaps are extracted from -ln(1-EQE) (Fig. 5e) to be 1.86 eV, 1.48 eV, and 1.20 eV for pure Se, 14% Te, and 30% Te. The value for pure Se is consistent with previous estimates, and the high bandgap tunability through Te alloying is again apparent.

The dark *J*–*V* characteristics of the devices are plotted on a semi-log scale in Fig. 6a. Se is known to be highly resistive when not illuminated, which is reflected in the *J*–*V* curve.

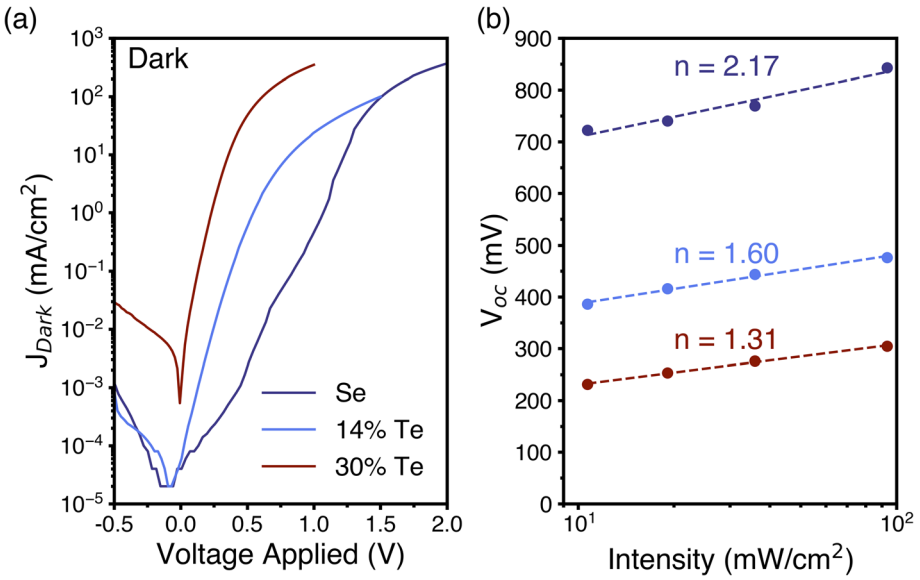

Fig. 6 Dark J–V electrical characterization and illumination-dependent V_{oc} as a function of Te concentration. (a) Semi-log J–V characteristics of cells measured under dark conditions. (b) Illumination-dependent V_{oc} and ideality factor fit.

Adding Te increases the current density under forward bias but also reduces the shunt resistance for 30% Te, which is detrimental to device performance. The high shunt conductance could result from Te-rich regions and/or the low (0.27 V) built-in potential. The high shunt conductance is consistent with previous work.[9,10]

We perform illumination intensity-dependent J–V measurements of representative devices and extract the ideality factor using the illumination dependent V_{oc} method (Fig. 6b). The Se devices have an ideality factor ~2, indicating Shockley-Read-Hall (SRH) recombination dominates. It is also possible that the higher ideality factor and slight nonlinearity for Se is related to previously reported illumination-dependent mobility,[26] though this will become clearer with improved film and interface quality. Devices from both alloys exhibit an ideality factor below 2, indicating a mixture of bimolecular and SRH recombination mechanisms. The greater defect density of 14% Te films (Fig. S4) likely results in a higher ideality factor (1.60) than 30% Te (1.31). The trend of the ideality factors (decreasing with increasing Te content) is consistent with the slope of the linear region of the semi-log dark J–V curves in Fig. 6a.

The low V_{oc} and FF of $Se_{1-x}Te_x$ alloys is likely attributable to a combination of higher defect densities and low built in-voltages (Fig. S4). 30% Te cells have comparable (~4×10^{16} cm^{-3}) bulk defect densities to pure Se, but more interface states/doping. 14% Te cells have on the order of 2×10^{17} cm^{-3} bulk defects and 2×10^{19} cm^{-3} total defects, hence the poor performance. Te point defects in Se are benign,[27] so it is likely that the significant decrease in grain size introduces the higher defect densities. This would be consistent with a previous study indicating that Te alloying results in extended defects acting as electron traps.[28] The built-in potentials, 0.52 V and 0.27 V for 14% and 30% Te, respectively, are similar to the V_{oc} for these materials, indicating that engineering the V_{bi} could be necessary to aid charge separation and suppress dark current.

Because the films are processed from molecular ink, we cannot rule out the possibility of organic residues related to the propylammonium cation or solvents, possibly resulting in C, N, H, or O impurities. However, C and N point defects in Se have high formation energies and are unlikely to significantly contribute to defect densities.[29] O point defects would be shallow and H defects are self-compensating.[27] Further, the PA^+ cation is expected to be extremely volatile and unlikely to remain, and the poly-selenide chain is entirely inorganic. Therefore, it is unlikely that organic residues would significantly contribute to device performance. The extent to which organics remain and the general dependence of film morphology/device performance on the size of the alkylammonium cation may merit future studies.

To characterize the stability, unencapsulated devices are stored in the dark in ambient air and repeatedly measured over time. Fig. 7a shows the PCE of representative devices over time. Se cells exhibit an improved PCE after aging for 1–2 weeks and show no performance degradation after over 1 month. The improvement after aging is a well-known phenomenon for devices with a MoO_x HTL due to healing of oxygen vacancies and has previously been observed for Se cells.[23] While accelerated aging tests will eventually be needed for Se cells once they become more commercially feasible, our results show the benefit of Se's air stability. In contrast, the performance of $Se_{1-x}Te_x$ cells degrades with time, with greater degradation for higher Te content. Cells stored in N_2 do not show significant degradation for 30% Te and show improvement in the 14% Te cells (Fig. 7b), so the degradation mechanism can be attributed to Te oxidation. This is further supported by XPS analysis, which shows an increase in Te^{4+} content with aging in air compared to a N_2-filled glovebox (Fig. S7). These results suggest $Se_{1-x}Te_x$

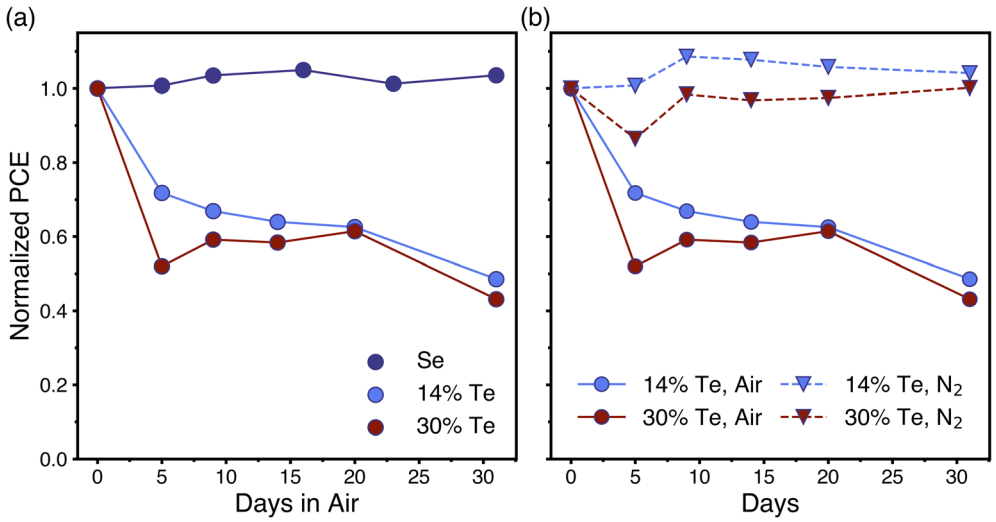

Fig. 7 Stability of Unencapsulated Devices. (a) Normalized PCE over time for devices stored in dark in air and remeasured over time. (b) Comparing the stability of $Se_{1-x}Te_x$ cells stored in air *vs.* stored in an N_2-filled glovebox over time. All devices are measured in air.

solar cells have the potential to be a stable technology, but alloys will likely require encapsulation.

Outlook and conclusions

Continued work to understand and control the crystallization process will be necessary to produce improved Se films with reduced defect densities. It is particularly important to understand intermediate phases and pathways between the PAPSe precursor and trigonal Se to tailor the ink, deposition, and annealing process. Understanding how to control the film formation with temperature, solvents, and additives will yield better device performance, but developing this understanding is a long process that is still ongoing for lead-halide perovskites after over a decade of research, for example. Work can also be done to improve the PAPSe precursor itself through optimized PA : ET : Se ratios and better precursor purification. Further, our results suggest that the TiO_2/Se interface is a limiting factor. Understanding the interactions between PAPSe and the TiO_2 and identifying an interfacial modification strategy could be fruitful in improving performance. For $Se_{1-x}Te_x$ alloys, the Te composition has a large impact on both bandgap and microstructure, meaning that the Te composition must be carefully tuned to optimize performance.

In summary, we have developed propylammonium poly-$[Se_{1-x}Te_x]_y^{2-}$ (PAPST) molecular inks as a promising precursor for hydrazine-free solution processing of Se and $Se_{1-x}Te_x$ thin films for photovoltaics. We have shown that thiol-amine solution processing can achieve comparable PCE for Se films (2.73%) to those processed by hydrazine, with higher open circuit voltage (up to 854 mV). Similarly, we achieve PCEs for $Se_{0.7}Te_{0.3}$ films of 2.33%, better than previous work on solution processed $Se_{0.7}Te_{0.3}$ films[10] and comparable to evaporated films.[8,9] Using PAPSe/PAPST precursors, neat films with a wide processing window can be achieved for widely tunable bandgaps (1.86 eV to 1.20 eV and possibly lower), highlighting the potential of this processing method and the $Se_{1-x}Te_x$ materials system for next-generation PVs and other optoelectronics.

Conflicts of interest

There are no conflicts to declare.

Data availability

All data is available from the corresponding author upon reasonable request.

Supplementary information: methods and Fig. S1–S7. See DOI: https://doi.org/10.1039/d5ta06459g.

Acknowledgements

D. J. and A. D. A. acknowledge primary support from the University of Pennsylvania Materials Research Science and Engineering Center (MRSEC) DMR-2309043 Seed program and partial support from both the Vagelos Institute for Energy Science and Technology and National Science Foundation (NSF) DMR-2429281. C. R. K acknowledges support from IMOD STC DMR-2019444. B. M. E. acknowledges support from the National Research Council Fellowship program. B. M. E. and N. R. G. gratefully acknowledge support from the Air Force Office of Scientific Research Grant #FA9550-24RYCOR011 and the Asian Office of Aerospace Research and Development (AOARD) within the Air Force Office of Scientific Research grant #24IOA046. C. L. recognizes partial support from Intel Corporation under the SRS program. This work was conducted in its majority at the Singh Center for Nanotechnology at the University of Pennsylvania, which is supported by the NSF National Nanotechnology Coordinated Infrastructure Program grant no. NNCI-2025608. The authors gratefully acknowledge the use of facilities and instrumentation (G2V Pico solar simulator and Cary UV-Vis Spectrophotometer) supported by the

Department of Materials Science and Engineering Departmental Laboratory at the University of Pennsylvania. The authors acknowledge the use of an XRD facility supported by the Laboratory for Research on the Structure of Matter and the NSF through the University of Pennsylvania NSF MRSEC DMR-2309043. This research used Electron Microscopy facilities of the Center for Functional Nanomaterials (CFN), which is a U.S. Department of Energy Office of Science User Facility, at Brookhaven National Laboratory under Contract No. DE-SC0012704.

References

1 C. E. Fritts, New Form of Selenium Cell, *Am. J. Sci.*, 1883, **26**(156), 465–472.
2 K. Wang, Y. Shi, H. Zhang, Y. Xing, Q. Dong and T. Ma, Selenium as a Photoabsorber for Inorganic-Organic Hybrid Solar Cells, *Phys. Chem. Chem. Phys.*, 2014, **16**(42), 23316–23319, DOI: **10.1039/c4cp02821j**.
3 R. Nielsen, T. H. Hemmingsen, T. G. Bonczyk, O. Hansen, I. Chorkendorff and P. C. K. Vesborg, Laser-Annealing and Solid-Phase Epitaxy of Selenium Thin-Film Solar Cells, *ACS Appl. Energy Mater.*, 2023, **6**(17), 8849–8856, DOI: **10.1021/acsaem.3c01464**.
4 I. Hadar, T. B. Song, W. Ke and M. G. Kanatzidis, Modern Processing and Insights on Selenium Solar Cells: The World's First Photovoltaic Device, *Adv. Energy Mater.*, 2019, **9**(16), 1–9, DOI: **10.1002/aenm.201802766**.
5 R. Nielsen, A. Crovetto, A. Assar, O. Hansen, I. Chorkendorff and P. C. K. Vesborg, Monolithic Selenium/Silicon Tandem Solar Cells, *PRX Energy*, 2024, **3**(1), 1, DOI: **10.1103/prxenergy.3.013013**.
6 Q. Liu, X. Wang, Z. Li, W. Lu, X. Wen, X. An and M. Feng, Standing 1D Chains Enable Efficient Wide-Bandgap Selenium Solar Cells, *Adv. Mater.*, 2024, **2410835**, 1–8, DOI: **10.1002/adma.202410835**.
7 X. An, Z. Li, X. Wang, W. Lu, X. Wen, M. Feng, Q. Liu, Z. Wei, J.-S. Hu and D.-J. Xue, Photovoltaic Absorber "Glues" for Efficient Bifacial Selenium Photovoltaics, *Angew. Chem., Int. Ed.*, 2025, **64**, e202505297, DOI: **10.1002/anie.202505297**.
8 J. Zheng, L. Fu, Y. He, K. Li, Y. Lu, J. Xue, Y. Liu, C. Dong, C. Chen and J. Tang, Fabrication and Characterization of ZnO/Se1-XTex Solar Cells, *Front. Optoelectron.*, 2022, **15**(1), 1–11, DOI: **10.1007/s12200-022-00040-5**.
9 I. Hadar, X. Hu, Z. Z. Luo, V. P. Dravid and M. G. Kanatzidis, Nonlinear Band Gap Tunability in Selenium-Tellurium Alloys and Its Utilization in Solar Cells, *ACS Energy Lett.*, 2019, **4**(9), 2137–2143, DOI: **10.1021/acsenergylett.9b01619**.
10 S. D. Deshmukh, C. K. Miskin, A. A. Pradhan, K. Kisslinger and R. Agrawal, Solution Processed Fabrication of Se-Te Alloy Thin Films for Application in PV Devices, *ACS Appl. Energy Mater.*, 2022, **5**(3), 3275–3281, DOI: **10.1021/acsaem.1c03896**.
11 C. Tan, M. Amani, C. Zhao, M. Hettick, X. Song, D. H. Lien, H. Li, M. Yeh, V. R. Shrestha, K. B. Crozier, M. C. Scott and A. Javey, Evaporated SexTe1-x Thin Films with Tunable Bandgaps for Short-Wave Infrared Photodetectors, *Adv. Mater.*, 2020, **32**(38), 1–8, DOI: **10.1002/adma.202001329**.
12 J. Wu, Z. Zhang, C. Tong, D. Li, A. Mei, Y. Rong, Y. Zhou, H. Han and Y. Hu, Two-Stage Melt Processing of Phase-Pure Selenium for Printable Triple-Mesoscopic Solar Cells, *ACS Appl. Mater. Interfaces*, 2019, **11**(37), 33879–33885, DOI: **10.1021/acsami.9b09572**.
13 M. Zhu, F. Hao, L. Ma, T. B. Song, C. E. Miller, M. R. Wasielewski, X. Li and M. G. Kanatzidis, Solution-Processed Air-Stable Mesoscopic Selenium Solar Cells, *ACS Energy Lett.*, 2016, **1**(2), 469–473, DOI: **10.1021/acsenergylett.6b00249**.
14 M. Zhu, Y. Deng, W. Liu and X. Li, Preparation of Se-Based Solar Cell Using Spin-Coating Method in Ambient Condition, *Chinese Phys. B*, 2018, **27**(1), 015202, DOI: **10.1088/1674-1056/27/1/015202**.
15 D. H. Webber, J. J. Buckley, P. D. Antunez and R. L. Brutchey, Facile Dissolution of Selenium and Tellurium in a Thiol-Amine Solvent Mixture under Ambient Conditions, *Chem. Sci.*, 2014, **5**(6), 2498–2502, DOI: **10.1039/c4sc00749b**.
16 J. W. Turnley and R. Agrawal, Solution Processed Metal Chalcogenide Semiconductors for Inorganic Thin Film Photovoltaics, *Chem. Commun.*, 2024, **60**(40), 5245–5269, DOI: **10.1039/d4cc01057d**.
17 J. W. Turnley, S. D. Deshmukh, V. M. Boulos, R. Spilker, C. J. Breckner, K. Ng, J. K. Y. Liu, J. T. Miller, H. I. Kenttämaa and R. Agrawal, A Selenium-Based "Alkahest": Reactive Dissolutions of Metals and Metal Compounds with n-Alkylammonium Polyselenide Solutions, *Inorg. Chem. Front.*, 2023, **10**(20), 6032–6044, DOI: **10.1039/d3qi01632c**.
18 S. D. Deshmukh, L. F. Easterling, J. M. Manheim, N. J. Libretto, K. G. Weideman, J. T. Miller, H. I. Kenttämaa and R. Agrawal, Analyzing and Tuning the Chalcogen-Amine-Thiol Complexes for Tailoring of Chalcogenide Syntheses, *Inorg. Chem.*, 2020, **59**(12), 8240–8250, DOI: **10.1021/acs.inorgchem.0c00597**.
19 C. H. Chung, S. H. Li, B. Lei, W. Yang, W. W. Hou, B. Bob and Y. Yang, Identification of the Molecular Precursors for Hydrazine Solution Processed CuIn(Se,S)2 Films and Their Interactions, *Chem. Mater.*, 2011, **23**(4), 964–969, DOI: **10.1021/cm103258u**.
20 E. Grison, Studies on Tellurium - Selenium Alloys, *J. Chem. Phys.*, 1951, **19**, 1109–1113.
21 R. Geick, E. F. Steigmeier and H. Auderset, Raman Effect in Selenium–Tellurium Mixed Crystals, *Phys. Status Solidi*, 1972, **54**(2), 623–630, DOI: **10.1002/pssb.2220540226**.
22 K. Shen, X. Wang, B. Xiao, F. Bao, Y. Xie, J. Wu, F. Guo, H. Zhu, Z. Li and Y. Mai, Oxygen-Assisted High-Temperature Deposition of High-Efficiency Trigonal Selenium Solar Cells, *Adv. Energy Mater.*, 2025, **2501930**, 1–10, DOI: **10.1002/aenm.202501930**.
23 T. K. Todorov, S. Singh, D. M. Bishop, O. Gunawan, Y. S. Lee, T. S. Gershon, K. W. Brew, P. D. Antunez and R. Haight, Ultrathin High Band Gap Solar Cells with Improved Efficiencies from the World's Oldest Photovoltaic Material, *Nat. Commun.*, 2017, **8**(1), 682, DOI: **10.1038/s41467-017-00582-9**.

24 J. T. Heath, J. D. Cohen and W. N. Shafarman, Bulk and Metastable Defects in CuIn1-XGaxSe2 Thin Films Using Drive-Level Capacitance Profiling, *J. Appl. Phys.*, 2004, **95**(3), 1000–1010, DOI: **10.1063/1.1633982**.

25 B. Yan, X. Liu, W. Lu, M. Feng, H. J. Yan, Z. Li, S. Liu, C. Wang, J. S. Hu and D. J. Xue, Indoor Photovoltaics Awaken the World's First Solar Cells, *Sci. Adv.*, 2022, **8**(49), 1–8, DOI: **10.1126/sciadv.adc9923**.

26 R. S. Nielsen, O. Gunawan, T. Todorov, C. B. Møller, O. Hansen and P. C. K. Vesborg, Variable-Temperature and Carrier-Resolved Photo-Hall Measurements of High-Performance Selenium Thin-Film Solar Cells, *Phys. Rev. B*, 2025, **111**(16), 165202, DOI: **10.1103/PhysRevB.111.165202**.

27 S. R. Kavanagh, R. S. Nielsen, J. L. Hansen, R. S. Davidsen, O. Hansen, A. E. Samli, P. C. K. Vesborg, D. O. Scanlon and A. Walsh, Intrinsic Point Defect Tolerance in Selenium for Indoor and Tandem Photovoltaics, *Energy Environ. Sci.*, 2025, **18**, 4431–4446, DOI: **10.1039/d4ee04647a**.

28 X. Chen, S. Bai, R. Li, Y. Yang and Q. Lin, Resolving the Trap Levels of Se and Se1-XTex *via* Deep-Level Transient Spectroscopy, *Phys. Rev. Mater.*, 2024, **8**(3), 1–5, DOI: **10.1103/PhysRevMaterials.8.033805**.

29 H. Moustafa, J. Kangsabanik, F. Bertoldo, S. Manti, K. S. Thygesen, K. W. Jacobsen and T. Olsen, Selenium and the Role of Defects for Photovoltaic Applications, *Phys. Rev. Mater.*, 2024, **8**(1), 15402, DOI: **10.1103/PhysRevMaterials.8.015402**.

